AGU PUBLICATIONS

JGR

Journal of Geophysical Research: Space Physics

RESEARCH ARTICLE
10.1002/2016JA023592

Key Points:
- The electron radiation belt flux peaks during the passage of HSS trailing-edge stream interface
- Counterintuitively, the peak flux occurs when the magnetosphere is in its most calm configuration
- The hazard from so-called killer electrons is maximized; at the same time, hazard from spacecraft surface charging is minimized

Correspondence to:
M. H. Denton,
mdenton@newmexicoconsortium.org

Citation:
Denton, M. H., and J. E. Borovsky (2017), The response of the inner magnetosphere to the trailing edges of high-speed solar-wind streams, *J. Geophys. Res. Space Physics*, *122*, 501–516, doi:10.1002/2016JA023592.

Received 14 OCT 2016
Accepted 12 DEC 2016
Accepted article online 17 DEC 2016
Published online 21 JAN 2017

The response of the inner magnetosphere to the trailing edges of high-speed solar-wind streams

M. H. Denton[1,2] and J. E. Borovsky[1,3]

[1]Center for Space Plasma Physics, Space Science Institute, Boulder, Colorado, USA, [2]New Mexico Consortium, Los Alamos, New Mexico, USA, [3]Climate and Space Sciences and Engineering, University of Michigan, Ann Arbor, Michigan, USA

Abstract The effects of the leading edge stream interface of high-speed solar-wind streams (HSSs) upon the Earth's magnetosphere have been extensively documented. The arrival of HSSs leads to significant changes in the plasmasphere, plasma sheet, ring current, and radiation belts, during the evolution from slow solar wind to persistent fast solar wind. Studies have also documented effects in the lower ionosphere and the neutral atmosphere. However, only cursory attention has been paid to the trailing-edge stream interface during the transition back from fast solar wind to slow solar wind. Here we report on the statistical changes that occur in the plasmasphere, plasma sheet, ring current, and electron radiation belt during the passage of the trailing-edge stream interface of HSSs, when the magnetosphere is in most respects in an extremely quiescent state. Counterintuitively, the peak flux of ~1 MeV electrons is observed to occur at this interface. In contrast, other regions of the magnetosphere demonstrate extremely quiet conditions. As with the leading-edge stream interface, the occurrence of the trailing-edge stream interface has a periodicity of 27 days, and hence, understanding the changes that occur in the magnetosphere during the passage of trailing edges of HSSs can lead to improved forecasting and predictability of the magnetosphere as a system.

1. Introduction

Since the first explanations for geomagnetic storms associated with so-called M regions on the Sun [e.g., *Bartels*, 1939; *Parker*, 1964; *Billings and Roberts*, 1964), there have been numerous studies of fast solar wind, its interaction with slow solar wind, and subsequent effects in the magnetosphere. The repeatability of these effects, with a 27 day period, allows some level of predictability and forecasting to take place. Attention has focused on the *onset* of storms and their effects, but not on the *duration* or time of *cessation* of the storm period. Since attention has focused on the leading edge of HSSs, there has been little-to-no work in determining possibilities of predicting and forecasting the effects of trailing edges.

High-speed solar-wind streams are features in the solar wind that contain plasma originating from coronal holes [e.g., *Burlaga*, 1974; *Gosling et al*., 1978; *Geiss et al*., 1995]. The speed of the plasma within these regions ("fast" solar wind) is typically greater than the speed of the plasma that originated from other regions of the Sun ("slow solar wind"). As a result of this difference in speed two distinct boundaries arise: (i) the "leading edge" of HSSs, where fast solar wind catches up with preceding slow solar wind, resulting in compression of the plasma and the formation of a corotation interaction region (CIR), and (ii) the "trailing edge" of HSSs where the fast solar wind outpaces the slow solar wind following it, leading to a region of rarefaction. The effects of the leading-edge interaction region and HSS upon the Earth's magnetosphere have been studied in detail in numerous previous studies since such structures are known to cause geomagnetic storms [e.g., *Tsurutani et al*., 2006; *Denton et al*., 2006; *Borovsky and Denton*, 2006; and *McPherron and Weygand*, 2006, and references therein). In contrast there have only been a few limited studies of trailing edges of HSSs [e.g., *Burlaga et al*., 1990; *Burton et al*., 1999; *Simunac et al*., 2010] since the arrival of this region of solar wind has not been directly linked to repeatable changes in the state of the magnetosphere.

A recent study used both data analysis and simulations to comprehensively describe the solar wind properties of trailing edges of HSSs [*Borovsky and Denton*, 2016a]. The study contrasted the leading edge and the trailing edge of HSSs. It was shown that critical locations within trailing edges of HSSs can be readily identified by using a combination of solar wind parameters, including the solar wind velocity, heavy-ion charge states, and solar wind entropy. One conclusion to be drawn from the study is that the magnetosphere is bathed in a distinct type of solar wind before, during, and after the arrival of a trailing edge. And since such structures are repeatable with a period of 27 days (as with the leading edge of a HSS), understanding the effects of the

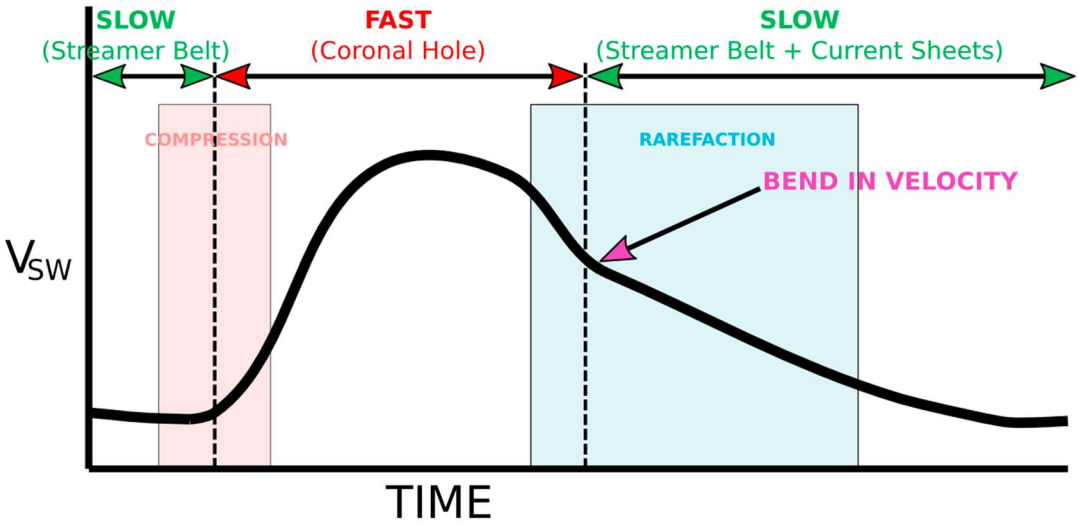

Figure 1. Schematic diagram of the leading edge and trailing edge of a high-speed solar wind stream. As fast solar wind catches up with the preceding slow wind it forms a compression region on the leading edge. The transition of the velocity back to slow solar wind results in a rarefaction region and a bend in the gradient of the velocity (also see *Borovsky and Denton* [2016a]). Changes in the state of the magnetosphere during the passage of the trailing edge have received little attention to date.

trailing edges on the magnetosphere will enhance our ability to predict and hence forecast the likely state of the magnetospheric system in advance. Predictions are of particular interest since the peak fluxes of the electron radiation belt occur during the passage of trailing edges of HSSs.

The work carried out in this current study is aimed toward extending the work of *Borovsky and Denton* [2016a] by considering the effects of trailing edges in the solar wind upon the plasmas and particle populations within the Earth's magnetosphere. Changes in the Earth's magnetic field are examined during the passage of trailing edges, along with changes in the plasmas of the magnetotail, the plasmasphere, the plasma sheet, the ring current, and the radiation belts. A combination of case studies and superposed epoch analyses are performed to explore the properties of the magnetosphere before, during, and after the arrival of trailing edges. Our findings document some of the effects of trailing edges of HSSs upon the magnetosphere and demonstrate that understanding these phenomena is important for developing a system-science view of the magnetosphere.

2. The Solar Wind Properties of Trailing Edges of HSSs

Figure 1 contains a schematic diagram of the solar wind velocity during the passage of a single HSSs, including the location of the compression region (CIR) on its leading edge and rarefaction region on its trailing edge (see also Figures 1, 2, and 5 from *Borovsky and Denton* [2016a]). The precise location of the interface between fast plasma that is of coronal-hole origin and slow plasma that originates in the streamer belt is generally straight-forward to identify on the leading edge of a HSS (e.g., the east-west flow deflection in the solar wind velocity), and challenging to identify on the trailing edge of a HSS. As outlined in *Borovsky and Denton* [2016a] a combination of parameters including the magnetic field strength, the intensity of the electron strahl, the orientation of current sheets, the intensity of the vorticity, the heavy-ion charge states, the proton specific entropy, and the solar wind velocity profile all show distinct signatures in the trailing edge rarefaction region. The authors in that study identified an inflection point in the solar wind velocity as the best indicator of the fast-to-slow-wind stream interface. Fluid simulations supported this parameter as marking the fast-to-slow transition based on pressure balance; see *Borovsky and Denton* [2016a Figures 11 and 12] for a detailed description of the fluid simulations. Based on the findings from that study, it is clear that during (and after) the arrival of trailing edges of HSSs in the vicinity of Earth, the magnetosphere will be bathed in a different type of solar wind, with different plasma parameters, than those which are encountered on the leading edge of HSSs.

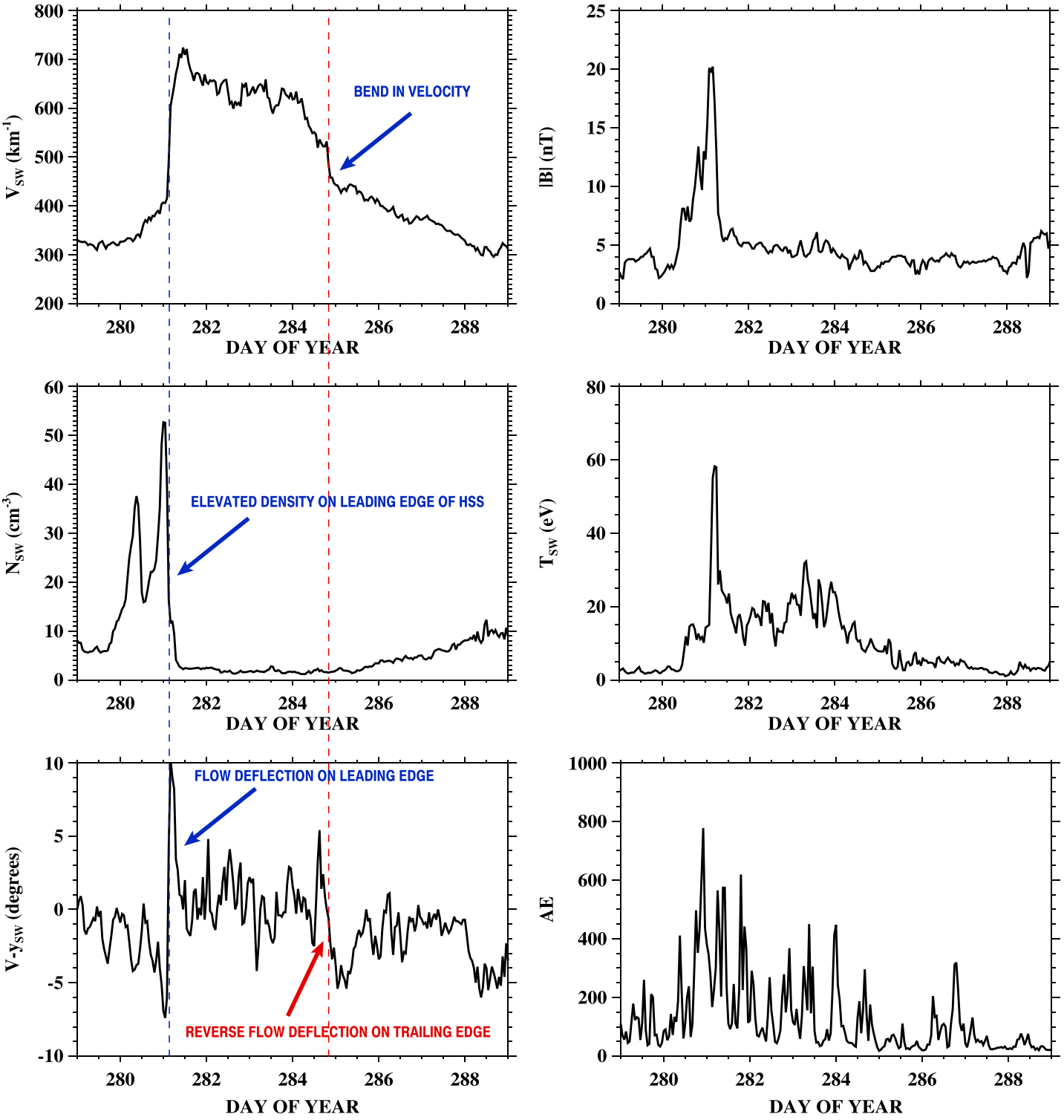

Figure 2. Assorted solar wind parameters and the *AE* index, taken from the OMNI2 database during a 10 day period containing the passage of a HSSs between 6 and 16 October 2005.

3. Case Study: 2–22 October 2005

The solar wind conditions during 10 days around the passage of a HSS in October 2005 are shown in Figure 2, along with the *AE* index. Clear signatures of the leading edge of the HSS are evident with an increase in solar wind density occurring prior to the arrival of fast wind ($V_{sw} > 600\,km\,s^{-1}$)—the density (and the magnetic field strength) increases due to fast wind catching up with preceding slow wind and generating a compression region. Noncompressive density structures also play a role in the pressure increase. The combination of high density, high solar wind speed, and increased magnetic field, all apparent in Figure 2, combine to drive activity in the magnetosphere before, during, and after the leading edge of a HSS. Such activity is particularly strong when the interplanetary magnetic field has a strong southwards component [cf. *McPherron et al*., 2009]. The transition from slow wind to fast wind on the leading edge of the HSS can be clearly identified by the east-to-west deflection in the flow velocity [*McPherron and Weygand*, 2006].

The particular event shown in Figure 2 is chosen as a case study due to the presence of a clear reverse west-to-east flow deflection in the *y* component of the velocity that occurs on the trailing edge of the HSS. It is noted that such west-to-east signatures are not always clearly evident for all trailing edges. However, also co-located with the reverse velocity deflection is an inflection in the solar wind velocity gradient. It is this signature (in many cases much easier to identify than changes in other parameters) that marks the fast-to-slow stream interface in the trailing edge of a HSS.

4. Data and Statistical Analyses

The data used in the current study are taken from a variety of sources. Changes in the bulk parameters of the solar wind are explored by using the OMNI2 database of solar wind observations [*King and Papitashvili*, 2005] at 1 h resolution. Solar wind composition during the passage of trailing edges is determined by using measurements from the Solar Wind Ion Composition Spectrometer (SWICS) instrument on board the ACE satellite [*Gloeckler et al*., 1998]. Changes in the magnetic field in the magnetosphere are determined from 1 min resolution magnetometer observations from the GOES spacecraft orbiting at geosynchronous orbit (GEO) [*Dunham et al*., 1996; *Singer et al*., 1996]. Plasma parameters (from ~1 eV to ~2 MeV) are provided by measurements from Los Alamos National Laboratory (LANL) spacecraft, also on orbit at GEO.

In order to reveal features that are common to the trailing edges of HSSs we first perform a statistical superposed-epoch analysis of a number of solar wind and plasma parameters from the inner magnetosphere during a collection of trailing-edge events. The events used are subselected from the original list of 54 trailing-edge events (1998–2008) given in Table 1 of *Borovsky and Denton* [2016a]. A subset of 43 events are identified where there was no arrival of a second HSS for at least 36 h after the time of the zero epoch. The time of the bend in the solar wind speed (change in gradient) is the zero epoch for the study [*Ilie et al*., 2008], since after consideration of a variety of other parameters, it was identified as the clearest boundary (stream interface) between the fast and slow solar winds [*Borovsky and Denton*, 2016a]. It is intended that the statistical analysis of these 43 events will reveal the reaction of the magnetosphere to the arrival and progression of a trailing edge alone, and the results will be uncontaminated by the subsequent arrival of known-storm drivers in the solar wind.

4.1. Solar Wind

Figure 3 contains plots of eight superposed parameters for the list of 43 trailing edges used in this study, at 1 h resolution. Four solar wind parameters are plotted in Figure 3 (left column) (solar wind velocity, v_{sw}; solar wind density, N_{sw}; solar wind ram pressure, P_{ram}; and solar wind proton temperature, T_{sw}), and four geomagnetic indices are plotted in Figure 3 (right column) (auroral electrojet index, *AE*; planetary *Kp* index; pressure-corrected disturbance storm time index, *Dst**; and polar cap index, PCI), with values for seven of the parameters taken from the OMNI2 database. The pressure-corrected *Dst** index is calculated based on the formula given in *Borovsky and Denton* [2013]. The mean and the median of each superposition are shown in black and blue with the upper and lower quartiles shown in red and purple, respectively. The grey shading indicates the standard deviation of the superpositions.

With regard to solar wind parameters plotted in Figure 3 (left column), the superposition of the solar wind velocity over this fortnight shows that prior to zero epoch the velocity was elevated above

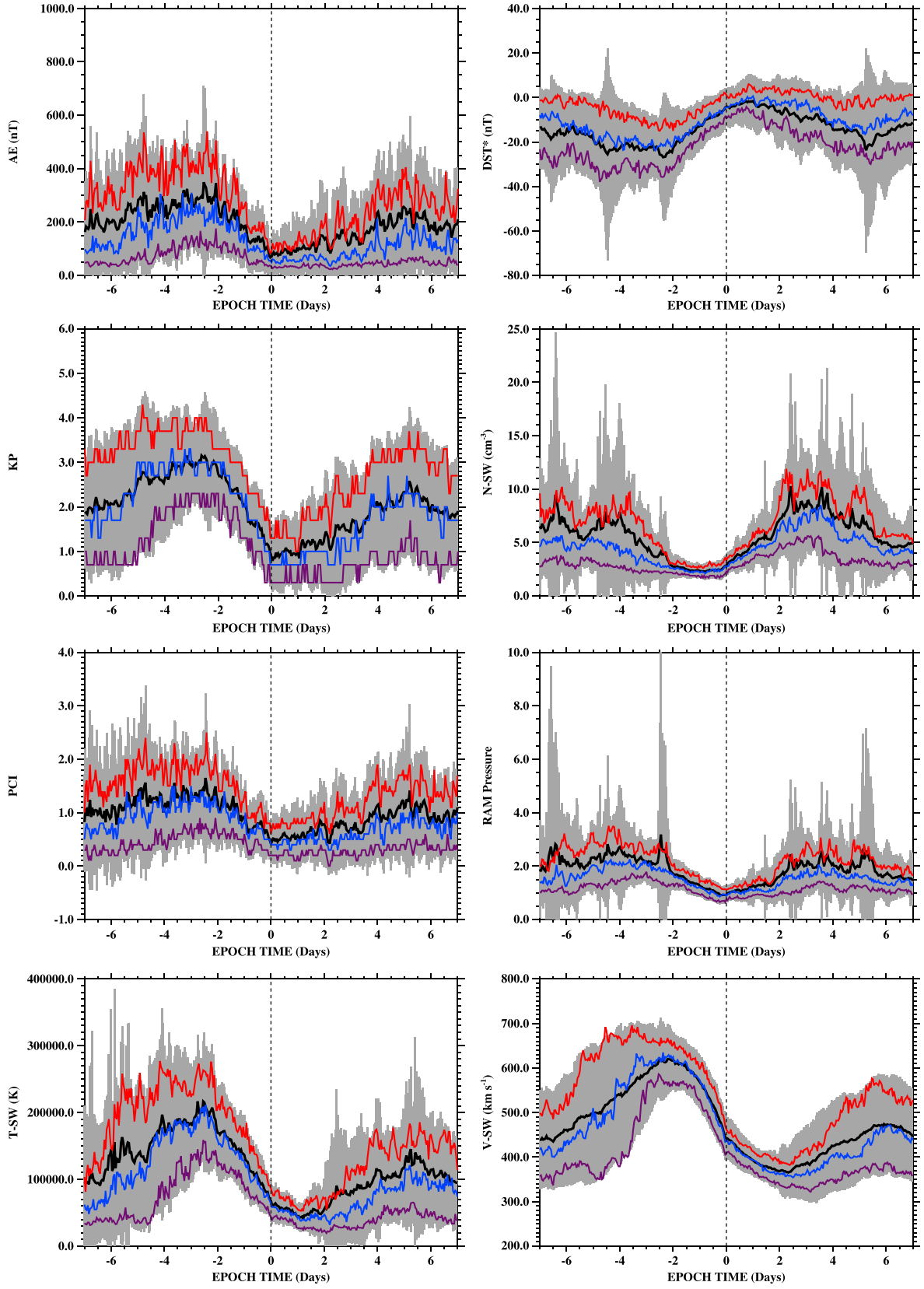

Figure 3. Superpositions of solar wind and magnetospheric parameters for 43 trailing edges of HSSs. The zero epoch for these events is the time of a clear change in the slope of solar wind speed as detailed in Table 1 of *Borovsky and Denton* [2016a].

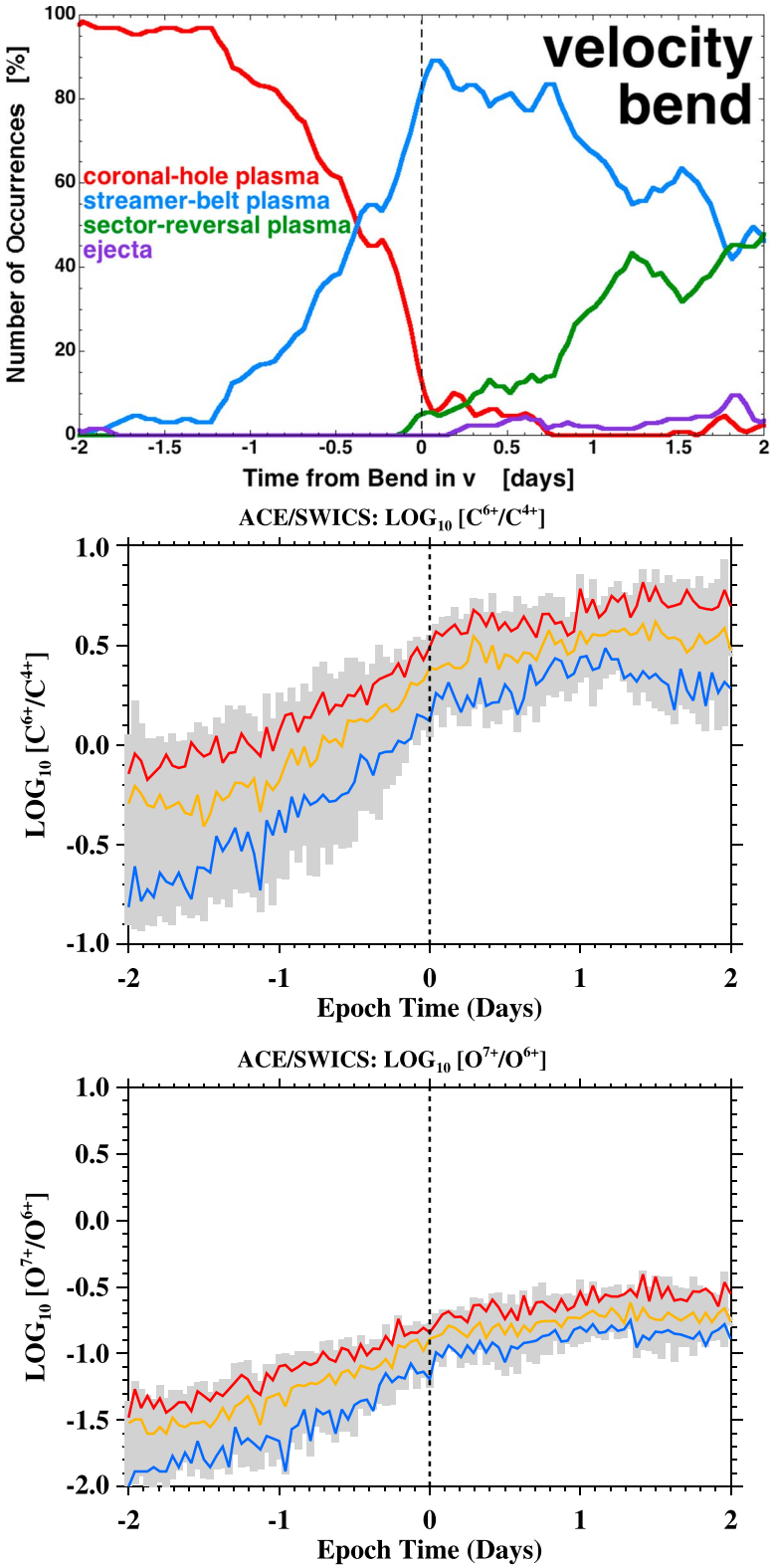

Figure 4. (top) A superposition of the solar wind categorization scheme of *Xu and Borovsky* [2015] applied to the 43 trailing edges of HSSs used examined in this study. Superpositions of heavy-ion charge-state ratios from the ACE/SWICS instrument are also shown. (middle) The C^{6+}/C^{4+} ratio and (bottom) the O^{7+}/O^{6+} ratio are also presented. The solar wind bathing the magnetosphere during trailing edges is much different than that bathing the magnetosphere during leading edges of HSSs.

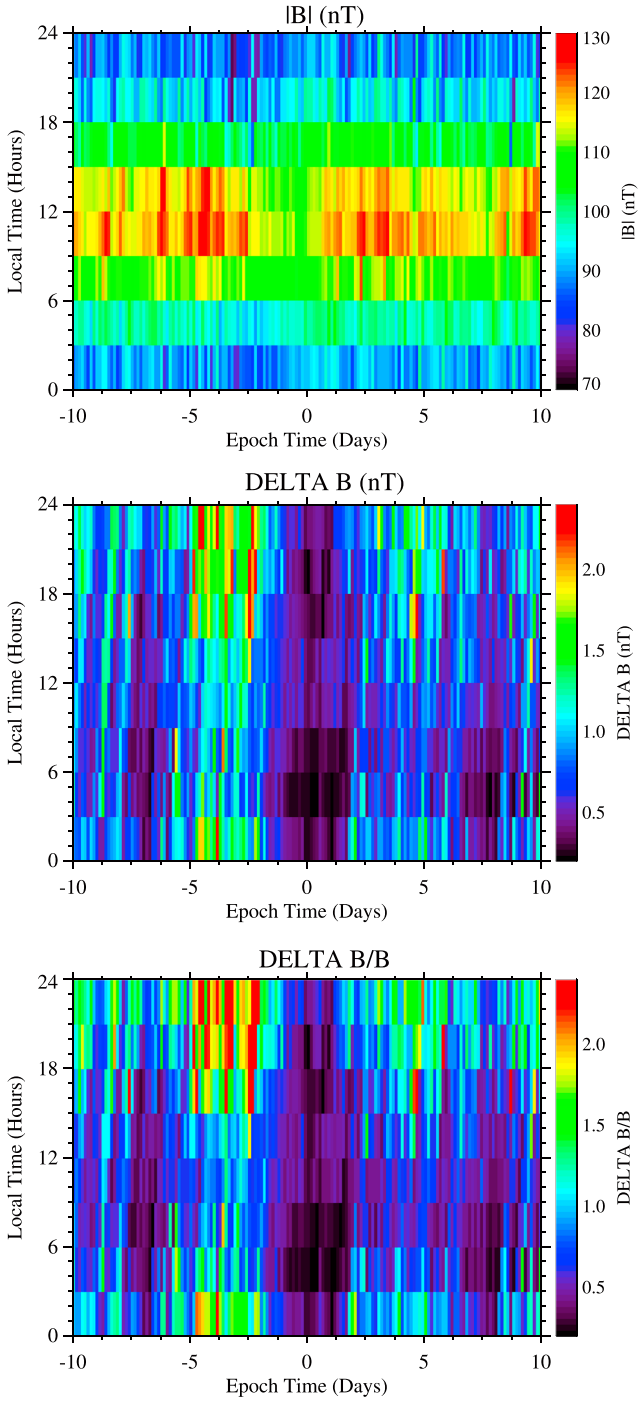

Figure 5. Superpositions of the measured magnetic field at GEO calculated from observations by GOES spacecraft during the passage of 43 trailing edges of HSSs. (top) The magnitude of the field, (middle) the 1 min change in the field, and (bottom) the normalized change in the field are plotted.

~550 km s^{-1} for ~6 days. At zero epoch a bend is evident in the velocity after which the velocity fall to between ~300 and 400 km s^{-1} for ~2–3 days. The solar wind number density prior to the zero epoch fluctuates around 3 cm^{-3} and then commences a gradual rise over the following 2–3 days. As a result of these density and velocity changes, the ram pressure of the solar wind is minimized (and reasonably symmetric) around zero epoch. The solar wind temperature is highest in the fast wind prior to zero epoch, falls approaching the stream interface, and continues falling over the following two days before commencing a gradual increase.

With regard to the terrestrial indices plotted in the right column, the *AE* index is elevated during the fast wind and then falls to a minimum at zero epoch, before rising slowly over the following days. The *Kp* index shows a similar trend with the highest activity occurring in the days prior to zero epoch, and the minimum activity occurring very close to the trailing-edge stream interface. Activity remains at very low levels for ~2–3 days after zero epoch. The pressure-corrected *Dst** index fluctuates around zero close to zero epoch and also remains at this level for ~2–3 days after zero epoch. The level of the PCI is very similar with the minimum occurring in the trailing-edge transition region. All geomagnetic indices demonstrate that while activity is elevated in the fast solar wind prior to the zero epoch, the passage of the stream interface marks the commencement of a period when geomagnetic activity falls to very low levels (and remains at very low levels for in excess of 48 h). With the arrival of a trailing-edge stream interface the magnetosphere enters a calm state, with low solar wind driving.

In order to explore the precise nature of the solar wind bathing the magnetosphere at this time we perform a superposed epoch analysis of the solar wind categorization scheme developed by *Xu and Borovsky* [2015]. This scheme assigns a category to the origin of the solar wind with a 1 h time cadence. The four categories of solar wind origin are (1) Ejecta, (2) Coronal Hole, (3) Sector Reversal, and (4) Streamer Belt. Figure 4 contains a plot of this superposition for the 43 events considered in Figure 3 (top row).

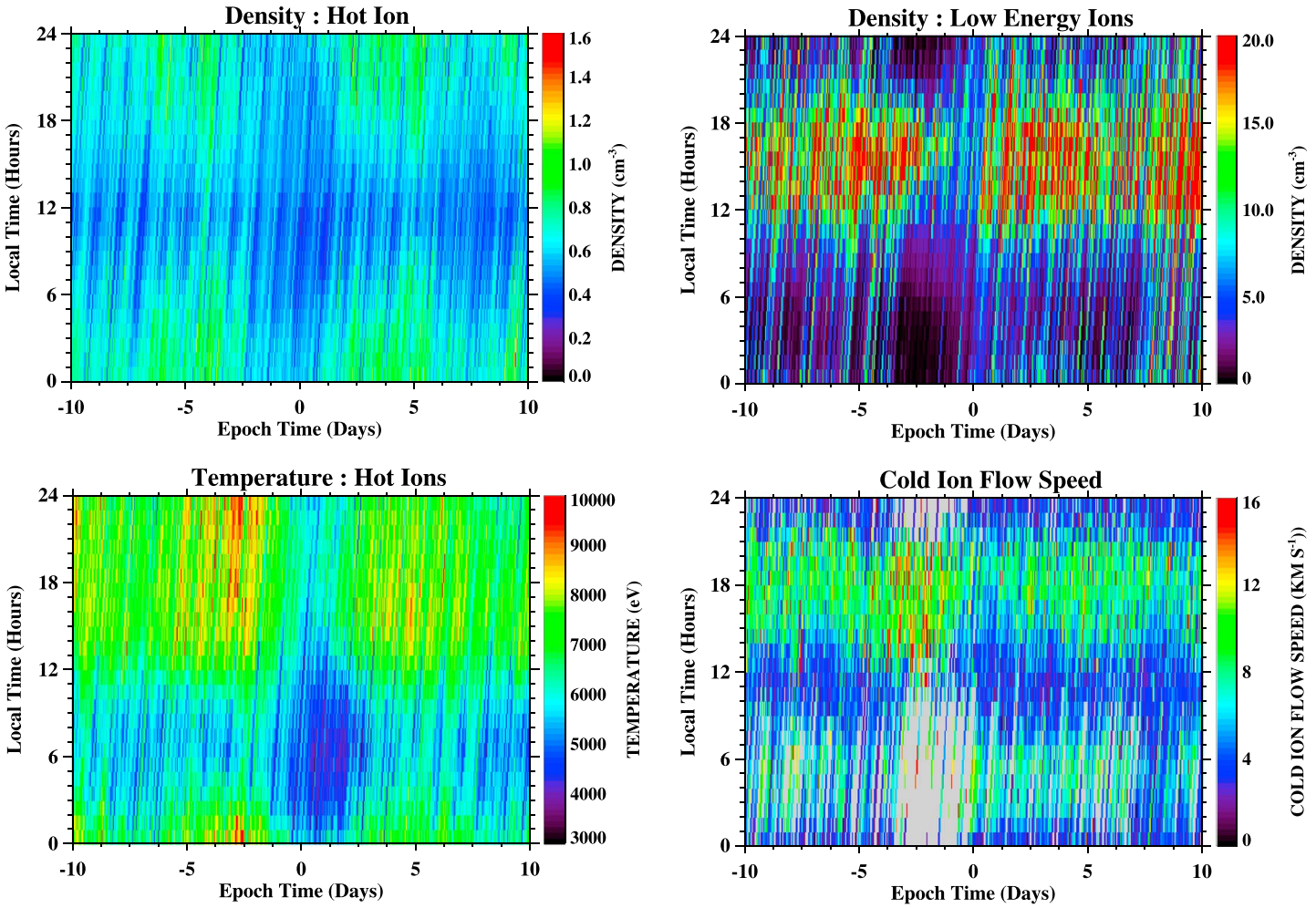

Figure 6. (left column) The superposed plasma sheet ion density and temperature, and (right column) the superposed plasmasphere density and flow speed, calculated from LANL/MPA observations during 43 trailing edges of HSSs.

Also shown in Figure 4 are charge-state ratios of the solar wind, the C^{6+}/C^{4+} ratio (Figure 3, middle row) and the O^{7+}/O^{6+} ratio (Figure 3, bottom row), from the SWICS instruement on board the ACE spacecraft [*Gloeckler et al*., 1998] previously examined in *Borovsky and Denton* [2016a]. The plots cover 4 days with the zero epoch being the time of the trailing edge of a HSS (bend in velocity). This plot demonstrates that the solar wind 2 days prior to zero epoch almost all originated in coronal holes (fast solar wind, as expected). The assigned origin of the solar wind then shifts in 24 h prior to the trailing edge to being streamer belt with some admixture of current-sheet origin solar wind. This categorization persists for the 2 days following the trailing edge.

The charge state ratios plotted in Figure 4 demonstrate similar gradients, showing a steady increase during the passage of the trailing edge. Since the charge state of the ions in the solar wind is a good marker for their origin on the Sun, these plots both demonstrate that the solar wind bathing the magnetosphere 48 h prior to the trailing edge is substantially different from the solar wind bathing the magnetosphere 48 h after the trailing edge has passed. Figure 3 also helps confirm that the events within the superpositions shown in Figure 3 are largely uncontaminated by known storm drivers (e.g., ejecta and fast solar wind from coronal holes) following zero epoch.

Taken together, the plots in Figures 3 and 4 demonstrate that the magnetosphere passes through a repeatable set of conditions during the passage of a HSS trailing edge. Examinations of the indices lead to the conclusion that the system is entering a period that would be considered very clam by most observers. However, it is unclear how this low driving manifests itself with regard to magnetospheric plasmas. Are the magnetic field and the plasmas of the magnetosphere also in a quiescent state?

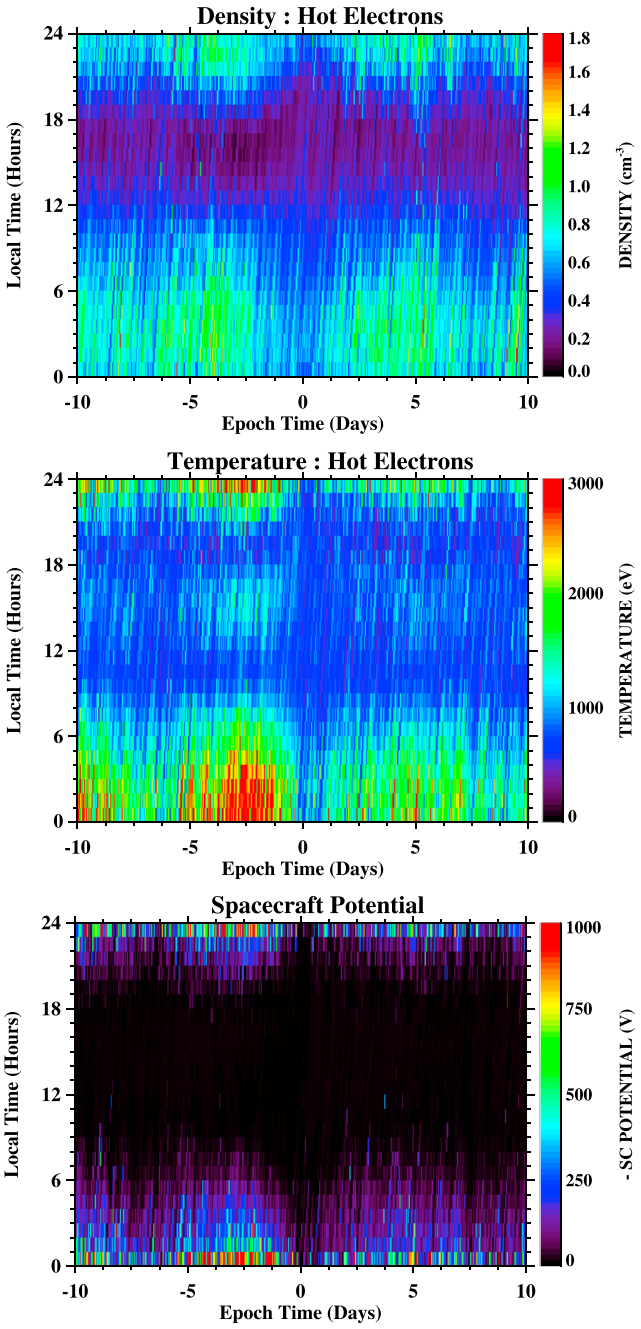

Figure 7. The (top) superposed plasma sheet electron density, (middle) temperature, and (bottom) negative spacecraft surface potential, calculated from LANL/MPA observations during 43 trailing edges of HSSs .

4.2. Magnetospheric Magnetic Field

The changes in magnetic field observed at GEO during the passage of the leading edge of a HSS have been investigated in detail by *Borovsky and Denton* [2010a] using magnetometer observations from the GOES spacecraft [*Dunham et al.*, 1996; *Singer et al.*, 1996]. Fluctuations in the magnetospheric magnetic field may drive radial diffusion of electrons in the outer radiation belt [e.g., *Fälthammar*, 1965; *Shprits et al.*, 2008a, 2008b] and/or energize these electrons [*Rostoker et al.*, 1998; *Mathie and Mann*, 2000; *Elkington et al.*, 2003]. On the leading edge of the HSS the increased density in the solar wind leads to compression of the magnetosphere and a sharp increase in the magnitude of the dayside field strength |**B**| and also a rapid increase in the field fluctuations [*Borovsky and Denton*, 2010a, 2016b]. Around 24 h after the passage of the leading edge of the HSS, the field magnitude declines but the field fluctuations continue whilever fast solar wind impinges on the magnetosphere. To investigate how the magnetospheric magnetic field at GEO changes during the trailing edges of HSSs, superposed parameters of the field magnitude, |**B**|, and the 1 min change in the field magnitude (defined as $\Delta B(t) = B(t + 1\ \text{min}) - B(t)$) are plotted in Figure 5 [*Dunham et al.*, 1996; *Singer et al.*, 1996]. It is apparent that the magnitude of the field around noon is, on average, reduced for ~24–48 h prior to the arrival of the trailing edge stream interface (~105 nT) compared with the usual noon field magnitude (~120 nT). The field magnitude increases back to this level at the same time as the arrival of the trailing edge, close to zero epoch. In contrast, fluctuations in the field magnitude cease more than 24 h prior to the arrival of the trailing edge stream interface and remain minimized until at least 24 h after the stream interface has passed—this roughly corresponds to the period of rarefaction in the solar wind within the trailing edge. Given the cessation in field fluctuations, it is logical to assume that only minimal acceleration and/or diffusion of electrons in the outer belt could take place via field fluctuations during this period.

4.4. Plasmasphere and Plasma Sheet

The effects of the trailing edges on the plasmasphere and plasma sheet can be evaluated by examining plasma data measured at GEO by the Magnetospheric Plasma Analyzer (MPA) instruments onboard multiple

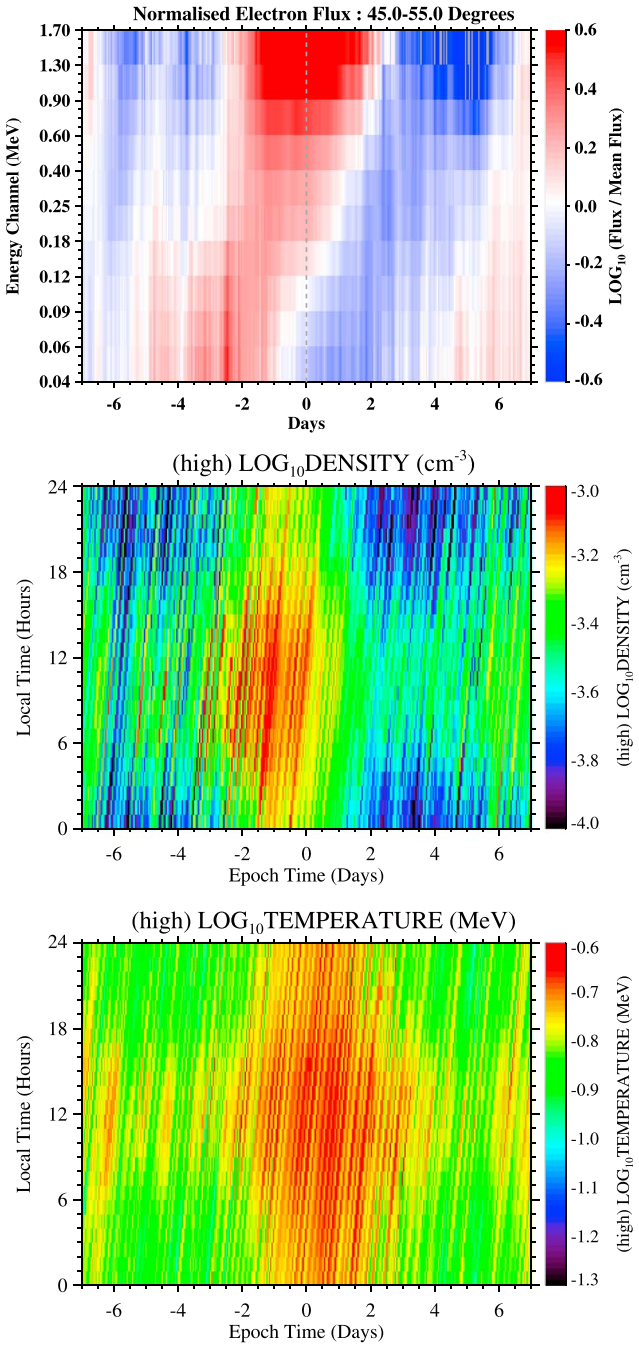

Figure 8. Superpositions of (top) the normalized superposed electron flux from the SOPA instrument, (middle) the electron density, and (bottom) the electron temperature, also from SOPA. The electron MeV flux peaks during the passage of the trailing edge, whilst the density peaks prior to the arrival of the trailing edge. The temperature (hardness) of the electron spectrum remains elevated for ~2 days after the passage of the trailing edge.

LANL satellites [*Bame et al.*, 1993]. MPA measures the distributions of ions and electrons from ~1 eV to ~40 keV [*Thomsen et al.*, 1999]. Calculation of moments of the distribution yield the density and temperature of the hot electron population (plasma sheet) and the hot and cold ion populations (plasma sheet and plasmasphere) [*Thomsen et al.*, 1999]. The flow velocity of the cold ion population is also obtained. The plasma sheet is known to respond strongly to the leading edge of HSSs, and these changes have been studied in detail [e.g., *Denton and Borovsky*, 2006, 2009] with an increase in particle precipitation also demonstrated statistically and during case studies [e.g., *Longden et al.*, 2008; *Sandanger et al.*, 2009; *Kavanagh et al.*, 2012; *Clilverd et al.*, 2013; *Rodger et al.*, 2007, 2010]. Prior to the arrival of the leading edge of the HSS an elevated region of solar wind density is encountered. Approximately 2 h later elevated densities are encountered in the electron and ion plasma sheet around local midnight at GEO [*Denton and Borovsky*, 2008].

In the plasmasphere the increase in magnetospheric convection close to the leading edge of the HSS leads to the erosion of the outer regions and the formation of a plasmaspheric drainage plume [e.g., *Moldwin et al.*, 1994; *Goldstein and Sandel*, 2005; *Borovsky and Denton*, 2006, 2008; *Goldstein et al.*, 2014]. Changes in particle populations closer to Earth, that are known to have close links to the plasmasphere (e.g., the ionosphere [*Denton et al.*, 2007; *Pokhotelov et al.*, 2010]) and the lower atmosphere [e.g., *Mlynczak et al.*, 2008, 2010a, 2010b; *McGranaghan et al.*, 2014] have also been identified.

In order to examine some aspects of the reaction of the plasma sheet and the plasmasphere to the arrival and passage of trailing edges, hot ion data from MPA instruments at GEO are again utilized. Figure 6 contains plots of the hot ion density and temperature as a function of local time and epoch time (for the 43 events from Figure 3), along with the cold ion density and the cold ion flow speed in the equatorial plane. The hot ion density decreases over ~48 h prior to the passage of the trailing edge stream interface as the level of convection decreases (the ion and electron plasma sheet densities and temperatures are very closely correlated with

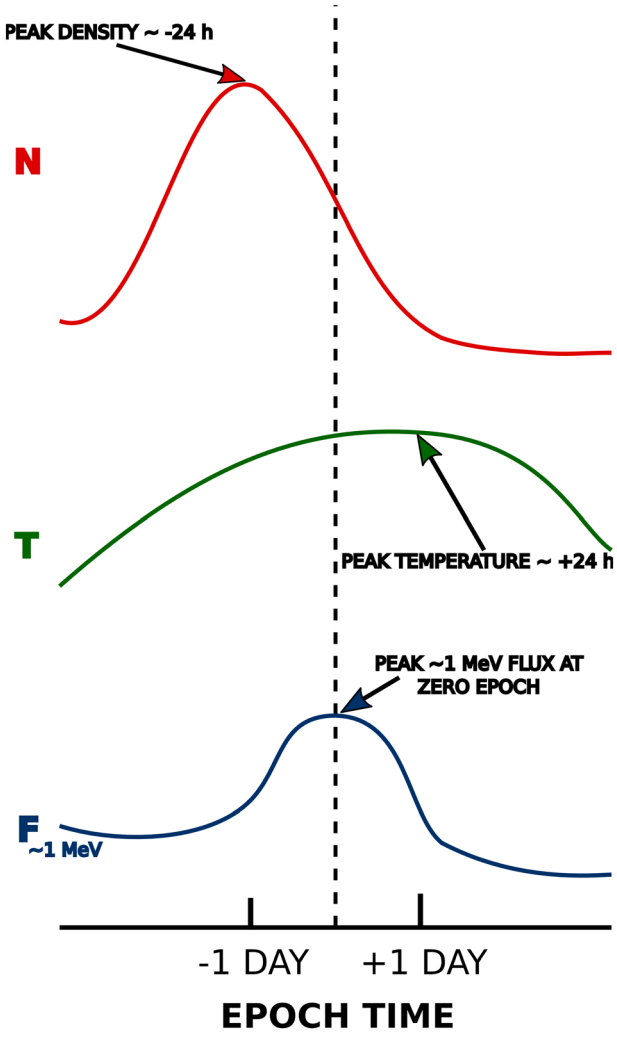

Figure 9. Schematic showing the behavior of the density *N*, temperature *T*, and flux *F*, during the passage of a leading edge stream interface and a trailing edge stream interface.

the level of convection). Prior to zero epoch convection has fallen to a very low level on average (cf. Figure 3) and the ion plasma sheet at this time has likely retreated radially outward beyond GEO. However, in the 24 h following zero epoch the plasma sheet is again detected at GEO with low density and low temperature. With respect to the cold ions of the plasmasphere, it is clear that during the ~4–5 day period of elevated solar wind speed during the HSS, and the concurrent high levels of convection, a high-density plasmaspheric drainage plume is detected at GEO (at ~18:00 LT). Flow speeds in the plume are typically sunwards [cf. *Borovsky and Denton*, 2008] with a magnitude of ~12–16 km s^{-1}. Prior to the trailing edge arrival, the density in the plume decreases and around zero epoch the flow speeds indicate a return to corotation of the plasma (flow speeds of ~8 km s^{-1}) maximized at dawn and dusk.

For comparison, the superposed hot electron density and temperature are shown in Figure 7, along with the measured (negative) spacecraft surface potential—a quantity known to be strongly correlated with the electron plasma sheet temperature [*Thomsen et al.*, 1999; *Denton et al.*, 2016]. Similar to the ion plasma sheet, the electron plasma sheet density and temperature decrease in the days prior to the arrival of the trailing-edge stream interface as magnetospheric convection falls to very low levels at this time. Around 24 h prior to zero epoch it is clear that the electron plasma sheet has retreated radially outward to beyond GEO and the density and temperature remain very low until ~24 h after zero epoch. It is apparent that the magnitude of the spacecraft potential measured by MPA is maximized during the passage of the HSS prior to the trailing edge when the electron temperature is high and the surface potential may reach thousands of volts (negative). For the 48 h period centered on zero epoch, the electron plasma sheet is outside of GEO and the measured surface potential is, on average, at very low levels.

4.5. Outer Radiation Belt

The leading edge of a HSS is known to frequently lead to dropouts in the outer electron radiation belt flux [e.g., *Freeman*, 1964; *Onsager et al.*, 2002, 2007; *Green et al.*, 2004; *Borovsky and Denton*, 2009b; *Morley et al.*, 2010] and phase-space density [e.g., *Hartley et al.*, 2013], and explanations of the dropout typically invoke some combination of magnetopause shadowing, outward radial diffusion, and particle precipitation [e.g., *Elkington et al.*, 2003; *Shprits et al.*, 2008a, 2008b; *Borovsky and Denton*, 2009a, 2009b; *Clilverd et al.*, 2013; *Turner et al.*, 2012; *Hartley and Denton*, 2014; *Rodger et al.*, 2016, and references therein]. Following the initial dropout, which occurs in close proximity in time to the leading edge of the HSS, the outer radiation belt recovers and electrons appear to be energized during the period of fast solar wind that follows the leading edge [*Borovsky and Denton*, 2010b]. Here we examine how the outer electron radiation belt measured at GEO

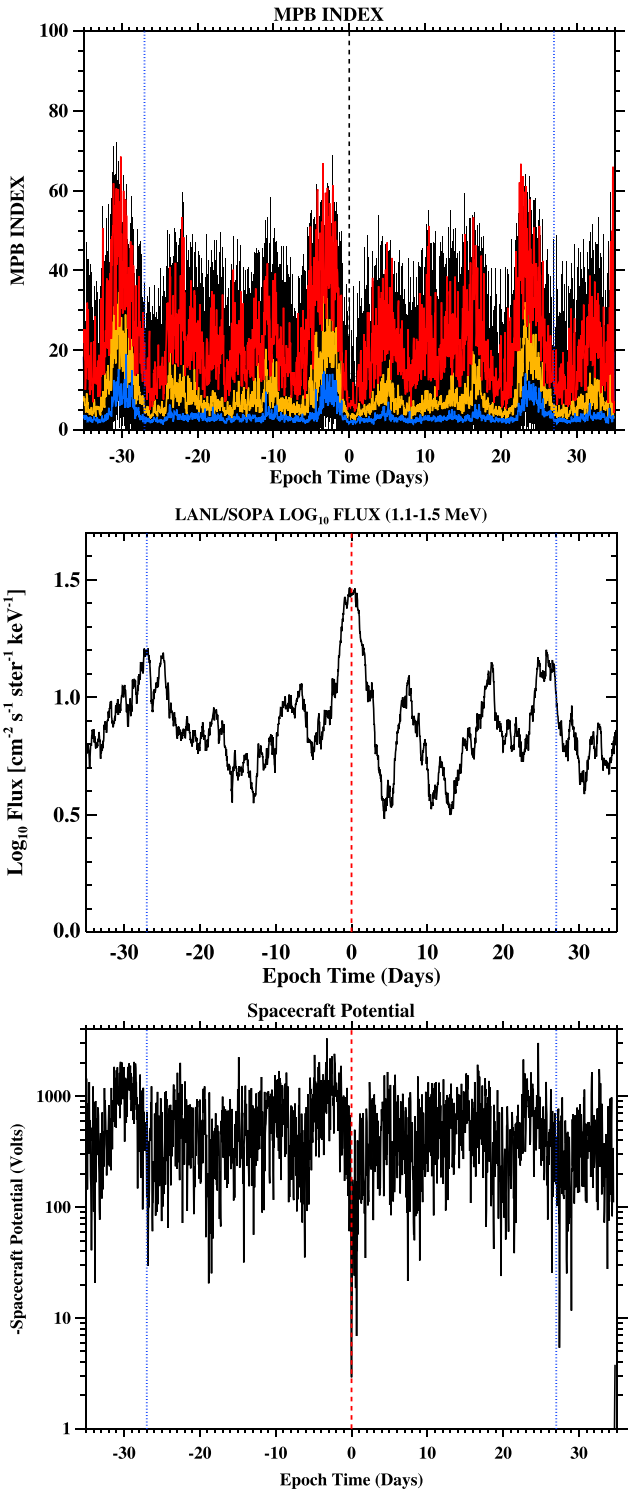

Figure 10. Superpositions of (top) the MPB index, (middle) the SOPA electron flux at 1.1–1.5 MeV, and (bottom) the measured MPA surface potentia. All parameters display a 27 day periodicity. The relativistic electron radiation belt flux is maximized at the time of the trailing edge; the spacecraft surface potential and the MPB index are minimized during the passage of the trailing edge.

responds during the passage of the trailing edge of a HSSs. Figure 8 contains plots of the normalized superposed electron flux measured by the LANL Synchronous Orbit Particle Analyzer (SOPA) instrument, also on orbit at GEO [*Belian et al.*, 1992; *Cayton and Belian*, 2007] for the same 43 events discussed above. Figure 8 (top) shows the normalized electron flux as a function of energy for pitch angles between 45 and 55°, averaged over all local times. The flux plotted here is normalized by the mean flux observed during the 35 days prior to zero epoch (cf. Figure 10). It is clear that the electron flux at the highest energies (MeV) is substantially increased in the days prior to zero epoch (when the fast solar wind in the HSS is passing the Earth). However, it is also apparent that the flux for the highest energies reaches a maximum very close to or just after the passage of the stream interface, before decreasing and then falling to lower levels over the following few days. The highest electron flux levels measured between 1.3 and 1.7 MeV occur in the 48 h centered on the trailing edge, when almost all measures of geomagnetic and solar activity are at their lowest levels. Interestingly, a recent study by *Hendry et al.* [2013] identified the same recovery-from-HSS storm period as the peak time for measured electron precipitation from the radiation belts into the atmosphere.

Figure 8 (middle and bottom) show the variation of the density and temperature of the electrons when relativistic bi-Maxwellian fits are made to the counts from the SOPA instrument. Previous results using this technique applied to the leading edge of HSSs demonstrated that important insights can be derived regarding the relativistic electron flux dropout and recovery [*Denton et al.*, 2010, *Borovsky and Cayton*, 2011; *Denton and Borovsky*, 2012; *Hartley et al.*, 2014]. Close to the leading edge of a HSS the flux at relativistic energies decreases sharply over a very short time scale (minutes). During

the recovery from dropout the temperature and density behave differently from the flux. The density recovers first in the hours following the dropout and the temperature recovers slowly [*Borovsky and Denton*, 2010a; *Denton et al*., 2010]—the radiation belt recovery from dropout on the leading edge of a HSS can be described as the return of a high-density lower energy population that is energized slowly (the temperature increases) over a period of days following the leading edge of the HSS. The plots shown in Figure 8 also reveal important differences between the flux behavior and the density-temperature behavior. Figure 8 (middle) demonstrates that the density is elevated in the days prior to the trailing edge. The density then begins to decrease around zero epoch and this decrease continues for ~48 h. The temperature shown in Figure 8 (bottom) is elevated prior to zero epoch and remains elevated through the passage of the trailing edge stream interface—the peak temperature at ~1 MeV occurs ~24 h after the trailing edge interface. In contrast to the density, the temperature does not begin to fall significantly until ~48 h after the passage of the trailing edge. A summary schematic of these changes is provided in Figure 9 where the gross behaviors of the relativistic electron flux, *F*; density, *N*; and temperature, *T*, in the outer radiation belt encountered at GEO, around the passage of a trailing edge, are summarized.

5. Repeatability of Trailing Edges and Their Effects on the Magnetosphere

In Figure 10 a superposition of the MPB index [*Chu et al*., 2015] is plotted for 35 days prior to the trailing edge and 35 days after the trailing edge. The MPB index is being developed to identify periods of substorm activity. However, here we use the index as a general measure of magnetospheric activity and also a proxy for the likelihood of a "seed population" of the electron radiation belt. The variation of the MPB index shows a clear 27 day periodicity centered on the time of zero epoch. The index peaks during the passage of HSSs, highlighting the frequent and recurrent substorms that occur during these solar wind drivers. The index is minimized very close to the passage of the trailing edge when the occurrence of substorms is infrequent. Figure 10 (middle) shows the superposition of the 1.1–1.5 MeV flux from the LANL/SOPA instrument [cf. *Borovsky and Denton*, 2009b, 2010b; *Denton et al*., 2010]. Again, there is a 27 day periodicity to the fluxes—however, in contrast to the MPB index, the peak in the SOPA flux is centered on the time of the trailing edge, very close to zero epoch. Figure 10 (bottom) shows the superposition of the spacecraft surface charging measured by LANL/MPA instruments within 1 h of local midnight [cf. *DeForest*, 1972; *Thomsen et al*., 2013; *Denton et al*., 2016]. Again, a clear 27 day periodicity is evident. The time of most elevated (and potentially dangerous) charging is in the period of fast wind prior to the trailing edge. The time when the spacecraft charging is at its lowest level (most benign) is precisely centered on the passage of the trailing edge stream interface at zero epoch. Both the radiation belt electron flux and the level of spacecraft charging are potential hazards to the operation of orbital assets. However, it is clear that for HSSs and HSS-driven storms, the peak in the radiation belt flux is maximized (and potentially most dangerous) at the trailing edge stream interface, whilst the level of surface charging is minimized (and most benign).

6. Discussion and Conclusions

It has previously been demonstrated that a "calm-before-the-storm" in the magnetosphere occurs prior to the arrival of HSSs [*Borovsky and Steinberg*, 2006; *Borovsky and Denton*, 2009a, etc] and such calms-before-storms have also been noted in activity within the Earth's ionosphere [*Clilverd et al*., 1993]. The transition from fast solar wind to slow solar wind that clearly occurs at the trailing edge stream interface of HSSs certainly marks the onset of a calm in geomagnetic (and solar) activity. However, whilst the magnetospheric magnetic field, the plasma sheet, and the plasmasphere evince little activity that could be considered "storm-like," the flux of relativistic electrons in the outer radiation belt reaches a peak. The hardness of the radiation belt spectra (temperature) as measured at GEO remains elevated actually continues to increase for ~48 h after the passage of the trailing edge. At a time when all geomagnetic and solar indices point to quiescent conditions, fluxes in the radiation belt are at a highly elevated level.

We conclude this study with a summary by enumerating the following points.

1. The solar wind impinging on the magnetosphere during the passage of trailing edges of HSSs is different to that during the leading edges of HSSs [see *Borovsky and Denton*, 2016a]. The effects of the trailing edge on magnetospheric plasmas have received little attention to date. This study has addressed this issue statistically and detailed some of the effects occuring during the passage of trailing edges.

2. The occurrence of trailing edges repeats with a 27 day period. Hence, understanding the changes in magnetospheric plasmas and related quantities provides some level of forecasting and predictability of the state of the magnetosphere 27 days after the passage of a trailing edge, and also some knowledge of the likely future state ~27 days in advance.
3. Solar wind and geomagnetic indices indicate that the magnetosphere is in many ways in a very quiescent state during the passage of a trailing edge. The trailing edge stream interface marks the beginning of a calm period of geomagnetic activity. Global magnetospheric convection, substorm activity, plasma sheet density, etc., are all at very low levels and have been quantified as a function of time relative to the passage of the trailing edge stream interface.
4. The plasma sheet electron temperature, as measured at GEO, is very low during the passage of the trailing edge. This results in minimal spacecraft surface charging, even in the region close to local midnight when the satellite is in darkness. Spacecraft anomalies related to surface charging will be less likely to occur under such conditions.
5. In contrast to other magnetospheric parameters investigated, the flux in the electron radiation belt reaches its peak very close to the time the trailing edge stream interface. The temperature (spectral hardness) in the outer radiation belt measured at GEO remains at an elevated level for more than 48 h after the passage of the stream interface. Such conditions may pose a risk to orbiting spacecraft.
6. Due to the connection between trailing edges measured at Earth, and their origin on the Sun, the physical behavior of the magnetosphere during the passage of trailing edges is repeatable with a 27 day periodicity, and hence predictable to some degree.
7. Since solar wind structures impinge on the planets situated radially inward and outward from Earth, the results from this study may have applications for understanding solar-wind/planetary coupling in other locations within the Solar System.

Acknowledgments
We gratefully acknowledge the ISR-1 group at Los Alamos National Laboratory for provision of the data from the MPA and SOPA instruments. Data are available by contacting the PI Mike Henderson at LANL (mghenderson@lanl.gov). Other spacecraft data are available via the NASA data servers http://cdaweb.gsfc.nasa.gov, http://omniweb.gsfc.nasa.gov, and http://omniweb.gsfc.nasa.gov/ and from the ACE data server http://www.srl.caltech.edu/ACE/ASC/. MHD wishes to thank Dan Welling for helpful suggestions during the preparation of this manuscript and Jo Denton for the help with preparation of some of the figures. This work was supported at the Space Science Institute by the NASA Heliophysics LWS program via grants NNX14AN90G and NNX16AB75G, the NASA Heliophysics GI program via grant NNX14AC15G, and the NSF GEM program award number 1502947.

References

Bame, S. J., D. J. McComas, M. F. Thomsen, B. L. Barraclough, R. C. Elphic, J. P. Glore, J. C. Chavez, E. P. Evans, and F. J. Wymer (1993), Magnetospheric plasma analyzer for spacecraft with constrained resources, *Rev. Sci. Instrum.*, *64*, 1026–1033, doi:10.1063/1.1144173.

Bartels, J. (1939), Some problems of terrestrial magnetism, in *Terrestrial Magnetism and Electricity*, pp. 385–433, McGraw Hill, New York and London.

Belian, R. D., G. R. Gisler, T. Cayton, and R. Christensen (1992), High-Z energetic particles at geosynchronous orbit during the Great Solar Proton Event Series of October 1989, *J. Geophys. Res.*, *97*(A11), 16,897–16,906, doi:10.1029/92JA01139.

Billings, D. E., and W. O. Roberts (1964), The origin of M-region geomagnetic storms, *Astrophys. Norv.*, *19*(16), 147–150.

Borovsky, J. E., and T. E. Cayton (2011), Entropy mapping of the outer electron radiation belt between the magnetotail and geosynchronous orbit, *J. Geophys. Res.*, *116*, A06216, doi:10.1029/2011JA016470.

Borovsky, J. E., and M. H. Denton (2006), The effect of plasmaspheric drainage plumes on solar-wind/magnetosphere coupling, *Geophys. Res. Lett.*, *33*, L20101, doi:10.1029/2006GL026519.

Borovsky, J. E., and M. H. Denton (2008), A statistical look at plasmaspheric drainage plumes, *J. Geophys. Res.*, *113*, A09221, doi:10.1029/2007JA012994.

Borovsky, J. E., and M. H. Denton (2009a), Electron loss rates from the outer radiation belt caused by filling of the outer plasmasphere: The calm before the storm, *J. Geophys. Res.*, *114*, A11203, doi:10.1029/2009JA014063.

Borovsky, J. E., and M. H. Denton (2009b), Relativistic electron dropouts and recovery: A superposed-epoch study of the magnetosphere and the solar wind, *J. Geophys. Res.*, *114*, A02201, doi:10.1029/2008JA013128.

Borovsky, J. E., and M. H. Denton (2010a), Magnetic field at geosynchronous orbit during high-speed stream-driven storms: Connections to the solar wind, the plasma sheet, and the outer electron radiation belt, *J. Geophys. Res.*, *115*, A08217, doi:10.1029/2009JA015116.

Borovsky, J. E., and M. H. Denton (2010b), On the heating of the outer electron radiation belt to produce high fluxes of relativistic electrons: Measured heating rates for high-speed-stream-driven storms, *J. Geophys. Res.*, *115*, A12206, doi:10.1029/2010JA015342.

Borovsky, J. E., and M. H. Denton (2013), The differences between storms driven by helmet streamer CIRs and storms driven by pseudostreamer CIRs, J. Geophys. Res. *Space Physics*, *118*, 5506–5521, doi:10.1002/jgra.50524.

Borovsky, J. E., and M. H. Denton (2016a), The trailing edges of high-speed streams at 1 AU, *J. Geophys. Res. Space Physics*, *121*, 6107–6140, doi:10.1002/2016JA022863.

Borovsky, J. E., and M. H. Denton (2016b), Compressional perturbations of the dayside magnetosphere during high-speed-stream-driven geomagnetic storms, *J. Geophys. Res. Space Physics*, *121*, 4569–4589, doi:10.1002/2015JA022136.

Borovsky, J. E., and J. T. Steinberg (2006), The "calm before the storm" in CIR/magnetosphere interactions: Occurrence statistics, solar wind statistics, and magnetospheric preconditioning, *J. Geophys. Res.*, *111*, A07S10, doi:10.1029/2005JA011397.

Burlaga, L. F. (1974), Interplanetary stream interfaces, *J. Geophys. Res.*, *25*, 3717–3725, doi:10.1029/JA079i025p03717.

Burlaga, L. F., W. H. Mish, and Y. C. Whang (1990), Coalescence of recurrent streams of different sizes and amplitudes, *J. Geophys. Res.*, *95*, 4247–4255, doi:10.1029/JA095iA04p04247.

Burton, M. E., M. Neugebauer, N. U. Crooker, R. von Steiger, and E. J. Smith (1999), Identification of trailing edge stream interfaces: A comparison of Ulysses plasma and composition measurements, *J. Geophys. Res.*, *104*, 9925–9932, doi:10.1029/1999JA900049.

Cayton, T. E., and R. D. Belian (2007), Numerical modeling of the Synchronous Orbit Particle Analyser (SOPA, Version 2) that flew on S/C 1990–095, LA Rep. LA-14335 Los Alamos Natl. Lab., Los Alamos, N. M.

Chu, X., R. L. McPherron, T.-S. Hsu, and V. Angelopoulos (2015), Solar cycle dependence of substorm occurrence and duration: Implications for onset, *J. Geophys. Res. Space Physics*, *120*, 2808–2818, doi:10.1002/2015JA021104.

Clilverd, M. A., T. D. G. Clark, A. J. Smith, and N. R. Thomson (1993), Observation of a decrease in midlatitude whistler-mode signal occurrence prior to geomagnetic storms, *J. Atmos. Terr. Phys.*, *55*, 1479–1485, doi:10.1016/0021-9169(93)90113-D.

Clilverd, M. A., N. Cobbett, C. J. Rodger, J. B. Brundell, M. H. Denton, D. P. Hartley, J. V. Rodriguez, D. Danskin, T. Raita, and E. L. Spanswick (2013), Energetic electron precipitation characteristics observed from Antarctica during a flux dropout event, *J. Geophys. Res. Space Physics*, *118*, 6921–6935, doi:10.1002/2013JA019067.

DeForest, S. E. (1972), Spacecraft charging at synchronous orbit, *J. Geophys. Res.*, *77*, 651–659, doi:10.1029/JA077i004p00651.

Denton, M. H., and J. E. Borovsky (2008), Superposed epoch analysis of high-speed-stream effects at geosynchronous orbit: Hot plasma, cold plasma, and the solar wind, *J. Geophys. Res.*, *113*, A07216, doi:10.1029/2007JA012998.

Denton, M. H., and J. E. Borovsky (2009), The superdense plasma sheet in the magnetosphere during high-speed-stream-driven storms: Plasma transport timescales, *J. Atmos. Sol. Terr. Phys.*, *71*, 1045–1058, doi:10.1016/j.jastp.2008.04.023.

Denton, M. H., and J. E. Borovsky (2012), Magnetosphere response to high-speed solar-wind streams: A comparison of weak and strong driving and the importance of extended periods of fast solar wind, *J. Geophys. Res.*, *117*, A00L05, doi:10.1029/2011JA017124.

Denton, M. H., J. E. Borovsky, R. M. Skoug, M. F. Thomsen, B. Lavraud, M. G. Henderson, R. L. McPherron, J. C. Zhang, and M. W. Liemohn (2006), Geomagnetic storms driven by ICME- and CIR-dominated solar wind, *J. Geophys. Res.*, *111*, A07S07, doi:10.1029/2005JA011436.

Denton, M. H., M. F. Thomsen, B. Lavraud, M. G. Henderson, R. M. Skoug, H. O. Funsten, J.-M. Jahn, C. J. Pollock, and J. M. Weygand (2007), Transport of plasma sheet material to the inner magnetosphere, *Geophys. Res. Lett.*, *34*, L04105, doi:10.1029/2006GL027886.

Denton, M. H., J. E. Borovsky, and T. E. Cayton (2010), A density-temperature description of the outer electron radiation belt during geomagnetic storms, *J. Geophys. Res.*, *115*, A01208, doi:10.1029/2009JA014183.

Denton, M. H., M. G. Henderson, V. K. Jordanova, M. F. Thomsen, J. E. Borovsky, J. Woodroffe, D. P. Hartley, and D. Pitchford (2016), An improved empirical model of electron and ion fluxes at geosynchronous orbit based on upstream solar wind conditions, *Space Weather*, *14*, 511–523, doi:10.1002/2016SW001409.

Dunham, W. D., S. A. MacIntyre, and C. R. Upton (1996), Design and performance of the GOES-8 high resolution magnetometer, *SPIE Proc.*, *2812*, 365.

Elkington, S. R., M. K. Hudson, and A. A. Chan (2003), Resonant acceleration and diffusion of outer zone electrons in an asymmetric geomagnetic field, *J. Geophys. Res.*, *108*(A3), 1116, doi:10.1029/2001JA009202.

Fälthammar, C.-G. (1965), Effects of time-dependent electric fields on geomagnetically trapped radiation, *J. Geophys. Res.*, *70*(11), 2503–2516, doi:10.1029/JZ070i011p02503.

Freeman, J. W. (1964), The morphology of the electron distribution in the outer radiation zone and near the magnetospheric boundary as observed by Explorer 12, *J. Geophys. Res.*, *69*, 1691–1723, doi:10.1029/JZ069i009p01691.

Geiss, J., G. Gloeckler, and R. von Steiger (1995), Origin of solar wind from composition data, *Space Sci. Rev.*, *72*, 49–60, doi:10.1007/BF00768753.

Gloeckler, G., et al. (1998), Investigation of the composition of solar and interstellar matter using solar wind and pickup ion measurements with SWICS and SWIMS on the ACE spacecraft, *Space Sci. Rev.*, *86*, 497–539, doi:10.1023/A:1005036131689.

Goldstein, J., and B. R. Sandel (2005), The global pattern of evolution of plasmaspheric drainage plumes, in *Inner Magnetosphere Interactions: New Perspectives From Imaging*, edited by J. L. Burch, M. Schulz, and H. Spence, 1 pp., AGU, Washington, D. C., doi:10.1029/159GM01.

Goldstein, J., M. F. Thomsen, and A. DeJong (2014), In situ signatures of residual plasmaspheric plumes: Observations and simulation, *J. Geophys. Res. Space Physics*, *119*, 4706–4722, doi:10.1002/2014JA019953.

Gosling, J. T., J. R. Asbridge, S. J. Bame, and W. C. Feldman (1978), Solar wind stream interfaces, *J. Geophys. Res.*, *83*, 1401–1412, doi:10.1029/JA083iA04p01401.

Green, J. C., T. G. Onsager, T. P. O'Brien, and D. N. Baker (2004), Testing loss mechanisms capable of rapidly depleting relativistic electron flux in the Earth's outer radiation belt, *J. Geophys. Res.*, *109*, A12211, doi:10.1029/2004JA010579.

Hartley, D. P., and M. H. Denton (2014), Solving the radiation belt riddle, *Astron. Geophys.*, *55*, 6.17–6.20, doi:10.1093/astrogeo/atu247.

Hartley, D. P., M. H. Denton, J. C. Green, T. G. Onsager, J. V. Rodriguez, and H. J. Singer (2013), Case studies of the impact of high-speed solar wind streams on the electron radiation belt at geosynchronous orbit: Flux, magnetic field, and phase space density, *J. Geophys. Res. Space Physics*, *118*, 6964–6979, doi:10.1002/2013JA018923.

Hartley, D. P., M. H. Denton, and J. V. Rodriguez (2014), Electron number density, temperature, and energy density at GEO and links to the solar wind: A simple predictive capability, *J. Geophys. Res. Space Physics*, *119*, 4556–4571, doi:10.1002/2014JA019779.

Hendry, A. T., C. J. Rodger, M. A. Clilverd, N. R. Thomson, S. K. Morley, and T. Raita (2013), Rapid radiation belt losses occurring during high speed solar wind stream driven storms: Importance of energetic electron precipitation, in *Dynamics of the Earth's Radiation Belts and Inner Magnetosphere*, *Geophys. Monogr. Ser.*, vol. 199, edited by D. Summers et al., pp. 213–223, AGU, Washington, D. C., doi:10.1029/2012GM001299.

Ilie, R., M. W. Liemohn, M. F. Thomsen, J. E. Borovsky, and J. Zhang (2008), Influence of epoch time selection on the results of superposed epoch analysis using ACE and MPA data, *J. Geophys. Res.*, *113*, A00A14, doi:10.1029/2008JA013241.

Kavanagh, A. J., F. Honary, E. F. Donovan, T. Ulich, and M. H. Denton (2012), Key features of >30 keV electron precipitation during high speed solar wind streams: A superposed epoch analysis, *J. Geophys. Res.*, *117*, A00L09, doi:10.1029/2011JA017320.

King, J. H., and N. E. Papitashvili (2005), Solar wind spatial scales in and comparisons of hourly Wind and ACE plasma and magnetic field data, *J. Geophys. Res.*, *110*, A02104, doi:10.1029/2004JA010649.

Longden, N., M. H. Denton, and F. Honary (2008), Particle precipitation during ICME-driven and CIR-driven geomagnetic storms, *J. Geophys. Res.*, *133*, A06205, doi:10.1029/2007JA012752.

Mathie, R. A., and I. R. Mann (2000), A correlation between extended intervals of ULF wave power and storm time geosynchronous relativistic electron flux enhancements, *Geophys. Res. Lett.*, *27*(20), 3261–3264, doi:10.1029/2000GL003822.

McGranaghan, R., D. J. Knipp, R. L. McPherron, and L. A. Hunt (2014), Impact of equinoctial high-speed stream structures on thermospheric responses, *Space Weather*, *12*, 277–297, doi:10.1002/2014SW001045.

McPherron, R. L., and J. Weygand (2006), The solar wind and geomagnetic activity as a function of time relative to corotating interaction regions, in *Recurrent Magnetic Storms*, edited by B. Tsurutani et al., pp. 125, AGU, Washington, D. C.

McPherron, R. L., D. N. Baker, and N. U. Crooker (2009), Role of the Russell McPherron effect in the acceleration of relativistic electrons, *J. Atmos. Sol. Terr. Phys.*, *71*(10–11), 1032–1044, doi:10.1016/j.jastp.2008.11.002.

Mlynczak, M. G., F. J. Martin-Torres, C. J. Mertens, B. T. Marshall, R. E. Thompson, J. U. Kozyra, E. E. Remsberg, L. L. Gordley, J. M. Russell III, and T. Woods (2008), Solar-terrestrial coupling evidenced by periodic behavior in geomagnetic indexes and the infrared energy budget of the thermosphere, *Geophys. Res. Lett.*, *35*, L05808, doi:10.1029/2007GL032620.

Mlynczak, M. G., L. A. Hunt, J. U. Kozyra, and J. M. Russell III (2010a), Short-term periodic features observed in the infrared cooling of the thermosphere and in solar and geomagnetic indexes from 2002 to 2009, *Proc. R. Soc. London, Ser. A*, *466*, 3409–3419, doi:10.1098/rspa.2010.0077.

Mlynczak, M. G., et al. (2010b), Observations of infrared radiative cooling in the thermosphere on daily to multiyear timescales from the TIMED/SABER instrument, *J. Geophys. Res.*, *115*, A03309, doi:10.1029/2009JA014713.
Moldwin, M. B., J. Howard, J. Sanny, J. D. Bocchicchio, H. K. Rassoul, and R. R. Anderson (1994), Plasmaspheric plumes: CRRES observations of enhanced density beyond the plasmapause, *J. Geophys. Res.*, *109*, A05202, doi:10.1029/2003JA010320.
Morley, S. K., R. H. W. Friedel, E. L. Spanswick, G. D. Reeves, J. T. Steinberg, J. Koller, T. Cayton, and E. Noveroske (2010), Dropouts of the outer electron radiation belt in response to solar wind stream interfaces: Global positioning system observations, *Proc. R. Soc. London, Ser. A*, *466*, 3329–3350, doi:10.1098/rspa.2010.0078.
Onsager, T. G., G. Rostoker, H.-. J. Kim, G. D. Reeves, T. Obara, H. J. Singer, and C. Smithtro (2002), Radiation belt electron flux dropouts: Local time, radial, and particle-energy dependence, *J. Geophys. Res.*, *107*(A11), 1382, doi:10.1029/2001JA000187.
Onsager, T. G., J. C. Green, G. D. Reeves, and H. J. Singer (2007), Solar wind and magnetospheric conditions leading to the abrupt loss of outer radiation belt electrons, *J. Geophys. Res.*, *112*, A01202, doi:10.1029/2006JA011708.
Parker, E. N. (1964), Dynamical properties of stellar coronas and stellar winds, Parts I and II, *Astrophys. J.*, *139*, 72–123, doi:10.1086/147740.
Pokhotelov, D., P. T. Jayachandran, C. N. Mitchell, and M. H. Denton (2010), High-latitude ionospheric response to co-rotating interaction region- and coronal mass ejection-driven geomagnetic storms revealed by GPS tomography and ionosondes, *Proc. R. Soc. London, Ser. A*, *466*, 3391–3408, doi:10.1098/rspa.2010.0080.
Rodger, C. J., M. A. Clilverd, N. R. Thomson, R. J. Gamble, A. Seppälä, E. Turunen, N. P. Meredith, M. Parrot, J. A. Sauvaud, and J.-J. Berthelier (2007), Radiation belt electron precipitation into the atmosphere: Recovery from a geomagnetic storm, *J. Geophys. Res.*, *112*, A11307, doi:10.1029/2007JA012383.
Rodger, C. J., M. A. Clilverd, A. Seppälä, N. R. Thomson, R. J. Gamble, M. Parrot, J. A. Sauvaud, and T. Ulich (2010), Radiation belt electron precipitation due to geomagnetic storms: Significance to middle atmosphere ozone chemistry, *J. Geophys. Res.*, *115*, A11320, doi:10.1029/2010JA015599.
Rodger, C. J., K. Cresswell-Moorcock, and M. A. Clilverd (2016), Nature's grand experiment: Linkage between magnetospheric convection and the radiation belts, *J. Geophys. Res. Space Physics*, *121*, 171–189, doi:10.1002/2015JA021537.
Rostoker, G., S. Skone, and D. N. Baker (1998), On the origin of relativistic electrons in the magnetosphere associated with some geomagnetic storms, *Geophys. Res. Lett.*, *25*(19), 3701–3704, doi:10.1029/98GL02801.
Sandanger, M., F. Søraas, M. Sørbø, K. Aarsnes, K. Oksavik, and D. Evans (2009), Relativistic electron losses related to EMIC waves during CIR and CME storms, *J. Atmos. Sol. Terr. Phys.*, *71*(10-11), 1126–1144, doi:10.1016/j.jastp.2008.07.006.
Shprits, Y. Y., S. R. Elkington, N. P. Meredith, and D. A. Subbotin (2008a), Review of modeling of losses and sources of relativistic electrons in the outer radiation belt I: Radial transport, *J. Atmos. Sol. Terr. Phys.*, *70*, 1679–1693, doi:10.1016/j.jastp.2008.06.008.
Shprits, Y. Y., D. A. Subbotin, N. P. Meredith, and S. R. Elkington (2008b), Review of modeling of losses and sources of relativistic electrons in the outer radiation belt II: Local acceleration and losses, *J. Atmos. Sol. Terr. Phys.*, *70*, 1694–1713, doi:10.1016/j.jastp.2008.06.014.
Simunac, K. D. C., A. B. Galvin, J. Barry, C. Farrugia, L. M. Kistler, H. Kucharek, M. A. Lee, Y. C.-M. Liu, E. Mobius, and M. A. Popecki (2010), Identifying the ends of high-speed streams near 1 AU with in situ data from STEREO/PLASTIC, *AIP Conf. Proc.*, *216*, 351.
Singer, H. J., L. Matheson, R. Grubb, A. Newman, and S. D. Bouwer (1996), Monitoring space weather with the GOES magnetometers, *SPIE Proc.*, *2812*, 299.
Thomsen, M. F., E. Noveroske, J. E. Borovsky, and D. J. McComas (1999), Calculating the moments from measurements by the Los Alamos Magnetospheric Plasma Analyzer LA-13566-MS, Los Alamos National Laboratory.
Thomsen, M. F., M. G. Henderson, and V. K. Jordanova (2013), Statistical properties of the surface-charging environment at geosynchronous orbit, *Space Weather*, *11*, 237–244, doi:10.1002/swe.20049.
Tsurutani, B. T., et al. (2006), Corotating solar wind streams and recurrent geomagnetic activity: A review, *J. Geophys. Res.*, *111*, A07S01, doi:10.1029/2005JA011273.
Turner, D. L., Y. Shprits, M. Hartinger, and V. Angelopoulos (2012), Explaining sudden losses of outer radiation belt electrons during geomagnetic storms, *Nat. Phys.*, *8*, 208–212, doi:10.1038/nphys2185.
Xu, F., and J. E. Borovsky (2015), A new four-plasma categorization scheme for the solar wind, *J. Geophys. Res. Space Physics*, *120*, 70–100, doi:10.1002/2014JA020412.